

# High Performance Humidity Fluctuation Sensor for Wearable Devices via a Bioinspired Atomic-Precise Tunable Graphene-Polymer Heterogeneous Sensing Junction

Jiang He,<sup>†,‡</sup> Peng Xiao,<sup>†</sup> Jiangwei Shi,<sup>†</sup> Yun Liang,<sup>†,‡</sup> Wei Lu,<sup>\*,†,§</sup> Yousi Chen,<sup>\*,§</sup> Wenqin Wang,<sup>||</sup> Patrick Théato,<sup>†,¶</sup> Shiao-Wei Kuo,<sup>#,¶</sup> and Tao Chen<sup>\*,†,‡,§</sup>

<sup>†</sup>Key Laboratory of Marine Materials and Related Technologies, Zhejiang Key Laboratory of Marine Materials and Protective Technologies, Ningbo Institute of Materials Technology and Engineering, Chinese Academy of Sciences, Ningbo 315201, China

<sup>‡</sup>University of Chinese Academy of Sciences, 19A Yuquan Road, Beijing 100049, China

<sup>§</sup>National Engineering Laboratory for Carbon Fiber Preparation Technology, Ningbo Institute of Materials Technology and Engineering, Chinese Academy of Sciences, 1219 Zhongguan West Road, Ningbo 315201, China

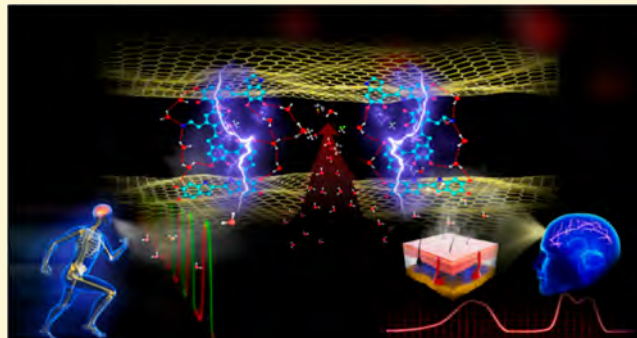
<sup>||</sup>Faculty of Materials Science and Chemical Engineering, Ningbo University, 818 Fenghua Road, Ningbo 315211, China

<sup>¶</sup>Institute for Technical and Macromolecular Chemistry, University of Hamburg, Bundesstrasse 45, D-20146 Hamburg, Germany

<sup>#</sup>Department of Material and Optoelectronic Science, National Sun Yat-Sen University, 804 Kaohsiung, Taiwan

## S Supporting Information

**ABSTRACT:** Measurements of an individual's water metabolism dynamical information can provide us rich biological information in a noninvasive way. This concept is hindered by the trade-off between the sensitivity and responsive velocity of traditional moisture sensors. Herein, inspired by the molecular detecting system based on weak bond interactions in natural organisms, we designed a new concept of a tunable graphene-polymer heterogeneous nanosensing junction by confining a reasonable thickness sensing material into graphene nanochannels. The fundamentally new sensing mechanism based on dynamical hydrogen bonds endows the sensor with over 4 orders of magnitude sensitivity toward a wide range of relative humidity (RH) (from 0% to 97%) with unprecedented fast response (20 ms) and recovery times (17 ms) with little humidity hysteresis. The promising advantages of the sensor allow us to record humidity fluctuation information in real time during a user's speech and breath, which can both reveal the speech feature and monitor the respiration rate accurately. Importantly, this advanced sensor provides a new opportunity for accurate and reliable physiological and psychological monitoring by detecting the subtlest RH fluctuations on human skin in a noncontact way.



## INTRODUCTION

Recently, wearable health monitoring devices are increasingly appealing in modern electronics, because they are capable of continuously recording physiological biomarkers of an individual human. Over the past decade, a large number of powerful wearable devices have been developed.<sup>1–5</sup> However, most of them can only enable real-time monitoring of an individual's physical activities and some vital signs (such as respiration rate, skin temperature and relative humidity, heart rate, and brain activity) by direct physical contact with applied pointers but fail to provide insight into the users' health state at molecular levels by noncontact and real-time detection of certain gas molecules diffusing from the human body.<sup>6–11</sup> Water is an indispensable substance to life on Earth and plays a vital role in human health. In this regard, water molecules can be suitable candidates of signal source, because of their extremely important role in most

humans' metabolism processes. Therefore, it is practically feasible to obtain physiological and psychological information on an individual through real-time monitoring of the content and distribution of water molecules around the human skin surfaces and exhaled air.<sup>12–16</sup> However, this promising approach has been neglected for wearable health monitoring applications for a long time, because there exist critical challenges of traditional humidity sensors for humidity fluctuation detecting, such as humidity hysteresis, stability, narrow sensing range, and the trade-off between the sensitivity and responsive velocity of the traditional moisture sensors,<sup>17–27</sup> which further hampered the real-time detection of this weak and dynamical biological

Received: April 16, 2018

Revised: June 10, 2018

Published: June 11, 2018

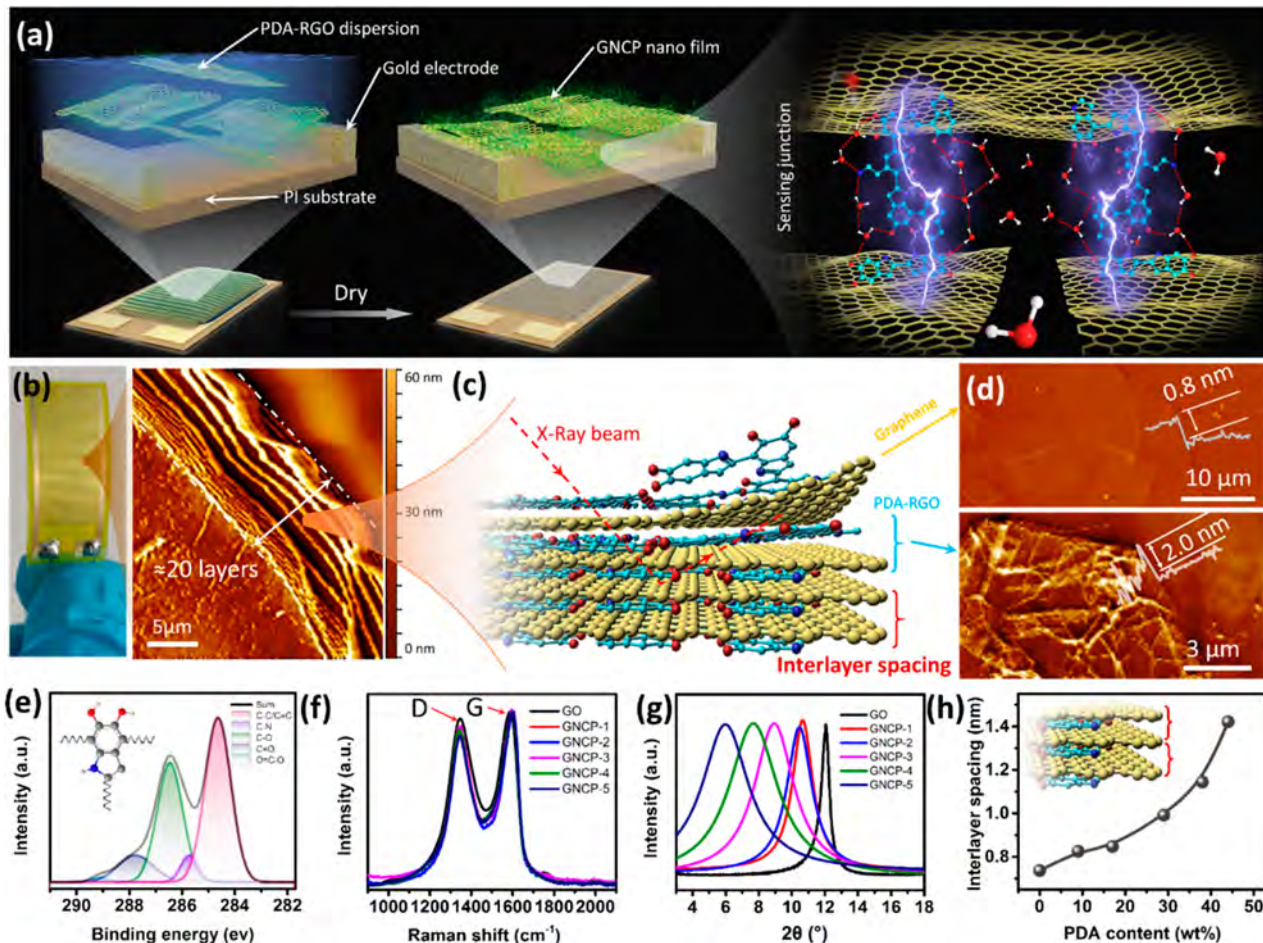


**Figure 1.** Fabrication and characterization of GNCP humidity sensors. (a) Schematic fabrication layer-by-layer stacking process of the GNCP high-order superlattice sensing junction structure. (b) Photograph of a drop-casted GNCP sensing element and AFM image of nanosize layered structure GNCP film on it. (c) Illustration of superlattices composed of alternating atomic scale PDA/graphene layers. (d) AFM image of graphene before (up) and after PDA modification (down). (e) XPS spectrum of the GNCP. (f) Raman spectra of GO and GNCP samples. (g) XRD patterns of GNCP with different RGO and PDA weight ratios. (h) The interlayer spacing due to the periodic and atomic scale tunable graphene sheet distance evaluated by XRD.

signal. Thus, the further development of a new sensing mechanism for the fabrication of a high performance humidity fluctuation sensor is significantly important.

A promising way to realize highly sensitive and fast moisture responsiveness is by mimicking the natural system. In natural organism systems, noncovalent intermolecular weak interactions play a crucial role in many biological interactions, including the interactions between proteins and other proteins and between proteins and other small molecules, providing the basis of how cells detect and respond to signals.<sup>28,29</sup> For instance, the human or some animal nose that takes advantage of various weak supramolecular interactions to bind a targeted odorant can realize odorant discrimination with an ultrahigh sensitivity of 0.1 femtomole (fM) within milliseconds.<sup>30,31</sup> Thus, it seems quite appealing to develop a bioinspired artificial moisture sensing system, which can bind low-concentration of water molecules in the environment via weak noncovalent interactions. Among various supramolecular interactions, hydrogen bonding is particularly interesting, because it is only of moderate strength (2–8 kcal/mol)<sup>32</sup> and thus undergoing constant breaking and formation at room temperature.<sup>33–36</sup> This unique dynamic feature makes hydrogen bonds promising interactions to construct functionalized devices with fast response. For example,

biological enzymes can function as fast as  $10^6$  times per second via hydrogen bonds.<sup>28</sup> Inspired by this, we speculate whether it is possible to fabricate a new sensitive moisture responsive device with ultrafast response, in that the sensory materials take advantage of reversible hydrogen bonds to bind water molecules.

Herein, we report a robust flexible high performance humidity sensing material with alternating poly(dopamine)/graphene layers, (graphene nanochannels confined poly(dopamine)-(GNCP)), the interlayer spaces of which can be continuously tuned from 0.7 to 1.4 nm. Owing to the atomically precise tunable structure, high specific surface area, which is critical for gas molecular absorption, and prominent electrical properties of graphene<sup>37–44</sup> and the numerous O/N-containing groups of nanometer thick polymer coating with PDA chains,<sup>45–48</sup> the hybrid materials can immediately “capture” water molecules at high RH via hydrogen bonds interaction and easily “release” water molecules at low RH with ultrafast speed.<sup>49</sup> Therefore, the sensor can experience a charge carrier transport occurring via proton hopping at low RH conditions and via a hydrogen bond network of water molecules<sup>50</sup> at high RH atmosphere, resulting in high sensitivity and ultrafast response over a very long operating range (RH = 0%–97%). The promising advantages of

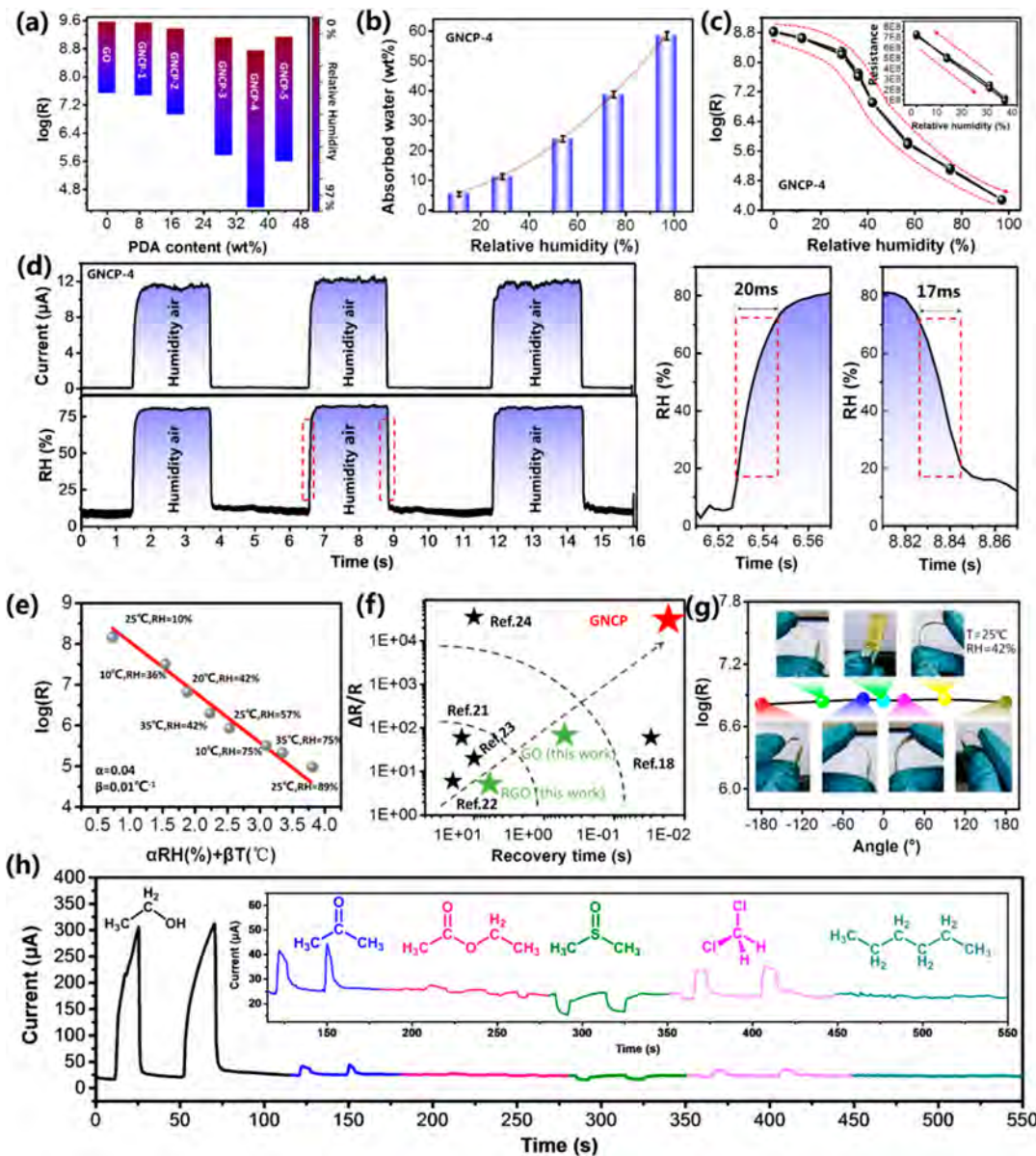


**Figure 2.** Quantitative study of the GNCP humidity sensor performance. (a) The RH (0% to 97%) depended resistance response range of GNCP sensors as a function of PDA content. (b) Histogram plots of absorbed water of GNCP-4 at different humidity atmospheres. (c) The derived RH-dependent resistance changes of GNCP-4 and its magnified curve of the low RH region from 0% to 35%. (d) The changes in the measured current from the film at 1 V as RH was switched between dry air ( $RH \approx 10\%$ ) and humidity air ( $RH \approx 80\%$ ) (right). Estimated results showed the ultrafast response (20 ms) and recovery (17 ms) times (left). (e) The approximate exponential behavior of resistance value vs humidity and temperature parameters according to the equation. (f) Comparison of sensitivity ( $\Delta R/R$ ) and recovery time of our GNCP sensor with that of many previously reported ones. (g) The device was bent to different angles and tested by the I–V curve under 1 V bias voltage. The results show no remarkable difference between the flat and bent states. (h) The sensor response to different organic vapor.

the sensor allow us to record the very weak and subtle ambient humidity fluctuations information caused by speaking, singing, and breathing, exercising, or even thinking and lying. Considering the facile and scalable preparation of the developed sensory materials as well as their powerful sensing ability, the proposed flexible moisture sensor holds great potential to be constructed as practically useful physiological and wearable psychological monitoring devices.

## RESULTS

### Fabrication and Characterization of GNCP Humidity Sensors.

Our strategy for fabricating bioinspired sensors of GNCP is schematically illustrated in Figure 1. As illustrated in

Figure 1a, dispersion of PDA modified GO (Figure S1)<sup>45,46</sup> was drop-casted on the commercially flexible PI substrates, which have been sputter-deposited with Ni/Au interdigital electrode (IDE) (Figure S2). After slowly evaporating the solvent at closed conditions ( $\approx 12$  h), the PDA-RGO nanosheets will spontaneously self-assemble into a 40 nm (Figure 1b, Figure 1c, and Figure S3) thick GNCP film in which monolayer graphene ( $\approx 0.8$  nm thick, Figure 1d-up) alternates with PDA molecular layers ( $\approx 1.2$  nm thick, Figure 1d-down)). Thus, abundant graphene-polymer heterogeneous sensing junctions with previously inaccessible structures in the GNCP material are formed. On the basis of the possible modulation of their conductive and sensory features, GNCP materials with different

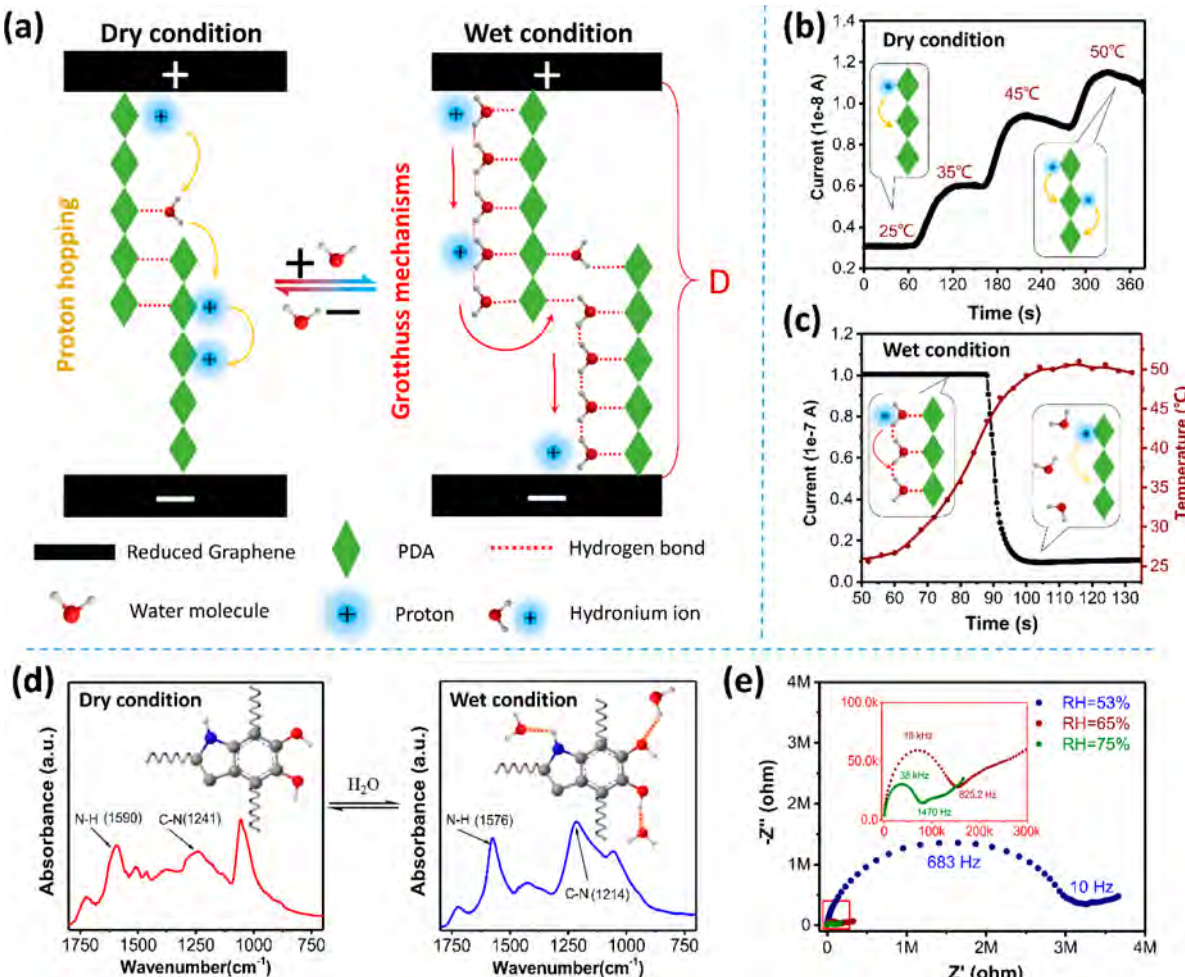


**Figure 3.** Sensing mechanism of the GNCP humidity sensor. (a) The possible mechanisms of proton transport in GNCP hybrid materials, including proton hopping mechanisms under low RH conditions (left) and Grotthuss mechanisms under high RH conditions (right). (b) The conductivity of the sensor increases with the rise of temperature under dry conditions ( $\text{N}_2$  atmosphere), which is a typical behavior in proton hopping conductors. (c) The conductivity of the sensor sharply decreases near a critical temperature point ( $\approx 45^\circ\text{C}$ ) at wet atmosphere ( $[\text{H}_2\text{O}] \approx 8858 \text{ ppm}$ ). (d) FTIR spectra of GNCP film under dry (left) and wet (right) atmospheres, respectively. (e) Nyquist plots of the impedance (imaginary part  $Z''$  versus real part  $Z'$ ) of an GNCP sensor at various RH conditions.

interlayer spacing and degree of reduction of GO were produced by carefully controlling the feed ratio of PDA to GO. As shown in Figure 1e, the XPS spectrum provides direct evidence of the successful attachment of PDA (285.8 eV, C–N bond) onto the surface of graphene. As seen in Figure 1f, the Raman spectroscopy shows that the D band intensity decreases as the PDA content increases, indicating the reduction of GO reduced by dopamine (Figure S4). Further analysis of the X-ray diffraction (XRD) patterns (Figure 1g) was used to determine the interlayer spacing of GNCP. The calculated results (Figure 1h) show that the interlayer spacing enlarges with increasing PDA content, thus the size of the sensing junction is controlled exactly by regulating the PDA content. Interestingly, above a critical point (37 wt %) of PDA content, the interlayer spacing increases more dramatically. Thus, by carefully controlling the PDA feeding content, the degree of reduction of GO and interlayer spacing of the sensing junction can be regulated precisely.

**Quantitative Study of the GNCP Humidity Sensor Performance.** Chemical architecture and nanoscale assembly are critical to optimizing proton transport in polymer materials.<sup>51</sup> Thus, the degree of reduction of GO and the

interlayer spacing of the sensing junction are two key factors that affect the sensor's performance. To screen the ideal sensory systems with satisfying detection sensitivity and fast response, the sensing features of the GNCP materials with varying PDA content were studied. Figure 2a presents the RH-dependent resistance response range of these sensory materials with different PDA content of 9 wt % to 44 wt %. Obviously, the widest resistance response range and relatively low resistance are observed for GNCP-4 with 37 wt % of PDA (Figure 2b). Therefore, GNCP-4 was chosen as a typical example and subjected to a systematical investigation. Figure 2c depicts the electric conductivity of GNCP-4 in different environmental RH. As can be seen, GNCP-4 is highly sensitive to variation of environmental humidity, as evidenced by the fact that its resistance has been improved by almost 4 orders of magnitude when the relative humidity changed from 0% to 97% with little hysteresis. At low RH range (<35%), the conductivity of GNCP-4 was very low. Interestingly, a sharp conductivity increase was noticed when RH reached over 35%. This may be attributed to a transition of the sensing mechanism. In particular, we have observed that the dependence of the resistance  $R$  on the RH relationship can be approximately described by two calibration

equations under dry and wet conditions (see Figure S5). Remarkably, the maximum sensitivity (defined as  $(R_{RH} - R_0)/R_0$  dry) of the as-established device can reach as high as 20000, which is significantly superior to GO or RGO humidity sensors. More importantly, its RH-dependent resistance plot (Figure 2c inset and Figure S5a) shows a good RH-resistivity linear correlation under low RH values (less than 35%), which is a clear advantage for low-humidity sensing tasks. Furthermore, in experiment observation, the dependence of the resistance value ( $R$ ) on RH and T parameters can be approximately described by an exponential relationship (Figure 2e).

Response and recovery time of GNCP-4, which is defined as the time to go from 10% to 90% of the high humidity value and vice versa, were also investigated. Figure 2d presents its response kinetics performance according to a reported method.<sup>17</sup> It shows that the response and recovery time of GNCP-4 are about 20 and 17 ms, respectively (Figure 2d-right), which are faster than most of the previously reported highly sensitive humidity sensors. It implies that the developed moisture sensor can not only perform with high sensitivity but also respond and recover with ultrafast speed compared to other types of humidity sensors (Figure 2f) (for a systematic comparison see Table S1).<sup>18–27</sup> More importantly, the small hysteresis property endows the sensor output stable square signal in fast continues humidity fluctuation detection process, which is critical for signal processing and accurate measurement in practical use. Considering that long-time storage may result in the conductivity change of the humidity sensor, the storage stability of GNCP-4 was also examined. In a typical experiment, GNCP-4 was stored in a closed chamber with constant humidity value ( $T = 25^\circ\text{C}$ , RH = 53%) for 60 days, and the I–V behaviors were then recorded. As shown in Figure S6a, it is found that the I–V behaviors of the present sensor keep nearly constant over time within experimental error, clearly demonstrating the satisfying stability of our sensor at room temperature.

Enlightened by the highly sensitive and ultrafast conductivity response of the GNCP-based flexible sensor to moisture, we investigated the possibility if the sensor may enable wearable health monitoring applications, for example, real-time recording of human exhaled air or the development of a wearable human skin humidity detecting device. Hence, their ability to withstand the stress of daily human wear and physical exercise was investigated, and the results are summarized in Figures 2g and S6b. It is obvious that the moisture sensing performance of the flexible sensor keeps almost constant within experimental error under different bending angles, demonstrating their potential as promising flexible wearable sensing devices. More interesting, the sensor can also respond to other volatile polar organic molecules (ethanol, acetone, ethyl acetate, dimethyl sulfoxide, dichloromethane) but in a different manner, indicating its great potential application in organic molecules sensing (Figure 2h).

**Sensing Mechanism of the GNCP Humidity Sensor.** As expected, the conductivity of the GNCP hybrid material is very sensitive to the variation of relative humidity environments, indicating its great potential as a smart humidity sensor. To gain insight into its moisture sensing mechanism, the effect of RH on the structure and properties of GNCP hybrid material was first studied. PDA polymer contains a large number of hydroxyl ( $-\text{OH}$ ) and amino groups ( $-\text{NH}_2$ ) that can act as proton donors and acceptors, providing a possible proton transport mechanism at low humidity by proton-hopping among the carboxyl and amino groups.<sup>52</sup> The presence of water molecules enables additional pathways of proton transport, beyond the

distance between two groups. Therefore, a slight increase in RH will significantly increase the conduct pathway and result in much enhanced conductivity of the GNCP hybrid material.<sup>53</sup> Consequently, this fact may enable water sensing at very low humidity conditions (Figure 3a-left). While at high RH, the Grotthuss mechanism of proton transport occurs via the formation and cleavage of hydrogen bonds wire or network<sup>50</sup> of water molecules (Figure 3a-right).<sup>54,55</sup> Since the activation energy of the Grotthuss mechanism ( $E_A \approx 0.11\text{ eV}$ ) is proved to be much lower than that of the proton-hopping mechanism ( $E_A = 0.5$  to  $0.9\text{ eV}$ ),<sup>53,56</sup> the more efficient Grotthuss-like proton transport pathway will dominate at high humidity levels.

Direct evidence for these two proton migration mechanisms comes from temperature-dependent proton conductivity experiments. As is known,<sup>57</sup> typical proton hopping type conduction complies with the following equation

$$\sigma = \frac{\sigma_0}{T} \exp\left(\frac{-E_A}{kT}\right)$$

where  $\sigma_0$  is a pre-exponential factor,  $k$  is the Boltzmann constant, and  $E_A$  is the activation energy. According to this equation, proton conductivity of the proton-hopping type mechanism is expected to increase with the increase of temperature, which agrees well with the experimental results obtained at low RH (Figure 3b). On the contrary, proton conductivity of the Grotthuss type mechanism should be much less sensitive to temperature variation at high RH, because it has a lower activation barrier for proton migration. However, it is worth noting that, similar to proteinase inactivation occurring at high temperature, the relatively weak hydrogen bonds “wire” or “network” in the GNCP sensor may also be destroyed at high temperature ( $>45^\circ\text{C}$ ), leading to the loss of water and essentially to a reduction of conductivity (more theoretical discussion is shown in Supporting Information Figure S7). As expected, as the temperatures reach a critical point ( $\approx 45^\circ\text{C}$ ), the conductivity of the samples sharply decreased by 1 order of magnitude (Figure 3c). Further quantitative analysis revealed that the resistance ( $\approx 10^8\Omega$ ) values at the critical temperature ( $45^\circ\text{C}$ ) in wet conditions is approximately equal to the values in dry conditions ( $\text{N}_2$  atmosphere) at the same temperature point, indicating a shift in the dominating conduction mechanism from the Grotthuss mechanism to the proton-hopping mechanism in high temperature conditions ( $>45^\circ\text{C}$ ).

FTIR studies were further used to confirm the above-mentioned moisture sensing mechanisms. As shown in Figure 3d, in the presence of water molecules, the original PDA absorption peaks at  $1590\text{ cm}^{-1}$  (N–H) and  $1241\text{ cm}^{-1}$  (C–N) shifted to  $1576$  and  $1214\text{ cm}^{-1}$ , respectively,<sup>49</sup> implicating that PDA does absorb water molecules via hydrogen bond interactions. Additionally, electrochemical impedance spectroscopy (EIS) of the sensory system was also conducted, because it is a very useful method to analyze the electrolyte ion transport and the electrochemical behavior. As shown in Figure 3e, there is a dramatic difference in Nyquist plots of the GNCP impedance spectrum at different RHs. For example, there is a semicircle at the high frequencies region connected with a long “tail” at the low frequencies region (mass transfer control region) in the impedance spectra at 65% and 75% RHs. This is consistent with typical spectrum of the Grotthuss mechanism, because it is the rate-limiting step.<sup>53,58</sup> In contrast, a much shorter “tail” is observed at relatively low RH (53%), which corresponds well to the proposed proton-hopping sensing mechanism, because it is an activation energy limiting pathway.

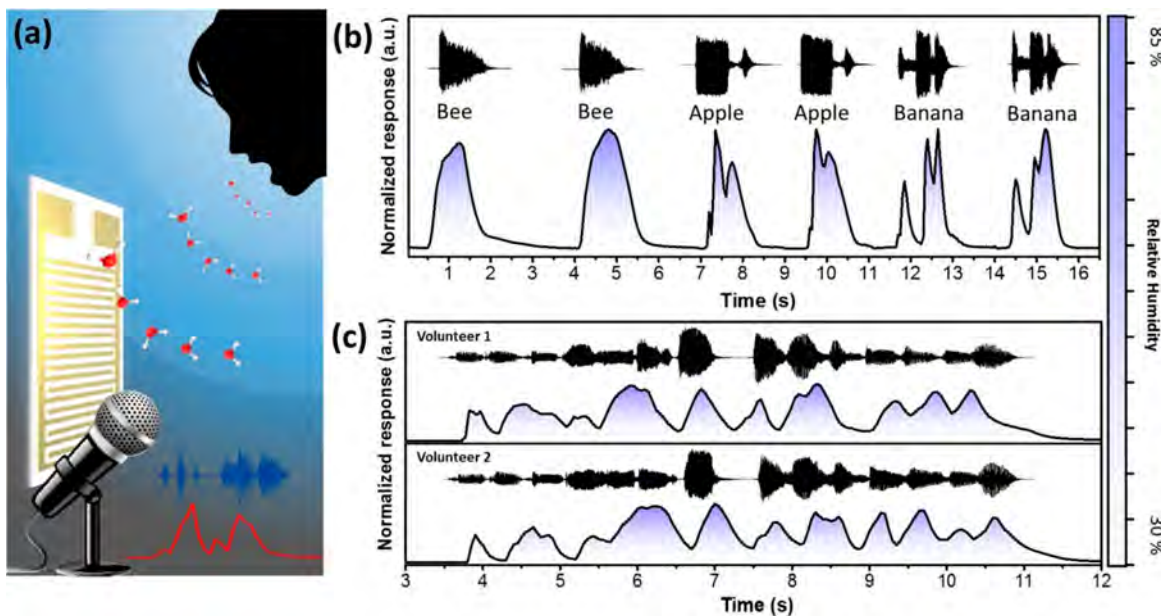


**Figure 4.** Humidity fluctuation information for voiceprint recognition anticontroling. (a) Schematic illustration of a humidity sensor for human exhaled air detection during speaking. (b) Repeated responses of a GNCP sensor to 3 different words. (c) Responses of a GNCP sensor to the song “Twinkle Twinkle Little Star” sung by two different volunteers.

**Humidity Fluctuation Information for Voiceprint Recognition Anticontroling.** Based on the promising results of the GNCP humidity sensor, the ability to develop a flexible sensor to record voice tones was then studied by singing and speaking to the flexible sensing device. As shown in Figure 4, when a person spoke (Figure 4b and Movie S1) or sang (Figure 4c) a portion of the song “Twinkle Twinkle Little Star”, the sensor was allowed to capture fine features of voice tones through real-time and ultrafast determination of the moisture variation during the person’s speech. These results successfully demonstrate the excellent ability of the flexible sensor to finely record human bioinformation features during speaking as well as singing. Although sound is a good signal for individual recognition in practical use (In fact, it has already been used in some areas, such as personal identification systems.), however, the human voice can be easily recorded, stored, and imitated by a machine (such as a computer and smartphone), thus rendering voiceprint recognition unsafe in practical use. As this complex dynamic humidity fluctuation information is hard for a machine to store and imitate, thus it may be helpful for voiceprint recognition anticontroling in practical use by combining humidity fluctuation information with voiceprint information.

**Humidity Sensor Application in Human Respiratory Monitoring.** Monitoring of respiratory information, such as respiratory rate, respiratory depth, and exhaled air components, has become a simple yet powerful noninvasive method to help assess the medical condition of a person and diagnose diseases. It is also an important index to evaluate training intensity for athletes and fitness enthusiasts. Water vapor is one of the most important components of exhaling air. Therefore, it should be possible to take advantage of the sensitive and fast-response moisture sensor to conduct accurate and facile recording of human respiration by noncontact and real-time determination of moisture variation around. Toward this end, we fabricated an efficient wireless wearable human breath real-time monitoring device. The device consisted of an GNCP humidity sensor and a

modified breath receiving mask (typically used for oxygen supply to patients). The signal of the sensor was then exposed to transduction, conditioning, and processing by a microcontroller and sent to a computer or an on-board wireless transceiver. The transceiver facilitates wireless data transmission to a Bluetooth-enabled smartphone for analysis or even uploads the data to cloud servers (Figure 5a, Figure 5b, and Movie S2). We have monitored the RH present in nasal breath instead of from mouth, as the former is a better representative measure of the lung hydration levels without interference from mouth saliva. When an individual breathes out into the mask, the exhaled airflow reaches the sensor and the RH value increased to  $RH_{Ex}$  immediately, thus generating an exhaled signal (green part of the breath curve in Figure S8). In reverse, when the individual inhales, the relative dry air flow in ambient air reaches the sensor and the RH value decreases to  $RH_{In}$  to generate an inhaled signal (red part of the breath curve of Figure S8). Thus, the respiratory signals can be divided into a series of intervals of exhaled and inhaled time sequence:  $(T_1^{Ex}, T_1^{In})$ ,  $(T_2^{Ex}, T_2^{In})$ ,  $(T_3^{Ex}, T_3^{In}) \dots (T_{n-1}^{Ex}, T_{n-1}^{In})$ ,  $(T_n^{Ex}, T_n^{In})$  (Figure S8). Hence, each time interval  $(T_n^{Ex}, T_n^{In})$  represents one complete breathing cycle from exhaling to inhaling, and the respiratory rate  $R_{res}$  in each breath cycle was deduced as follows:

$$R_{res} = \frac{60}{T_n^{Ex} + T_n^{In}} (\text{Breaths/min})$$

The smart mask was comfortable to wear on a volunteer face for a real-time respiratory monitoring data collection. The respiratory pattern of the volunteer was recorded in about 225 s with three different breathing states including slow, medium, and rapid. The obtained corresponding exhaled air RH value ( $RH_{In}$ ) and inhaled air RH value ( $RH_{Ex}$ ) and respiratory rate  $R_{res}$  data are shown in Figure 5c. To this end, a smart wireless mask is capable of monitoring simultaneously in real-time the exhaled flow humidity and respiratory rate fabricated successfully.

To validate performance under realistic conditions, the above setup was tested on different conditions. We first tested the

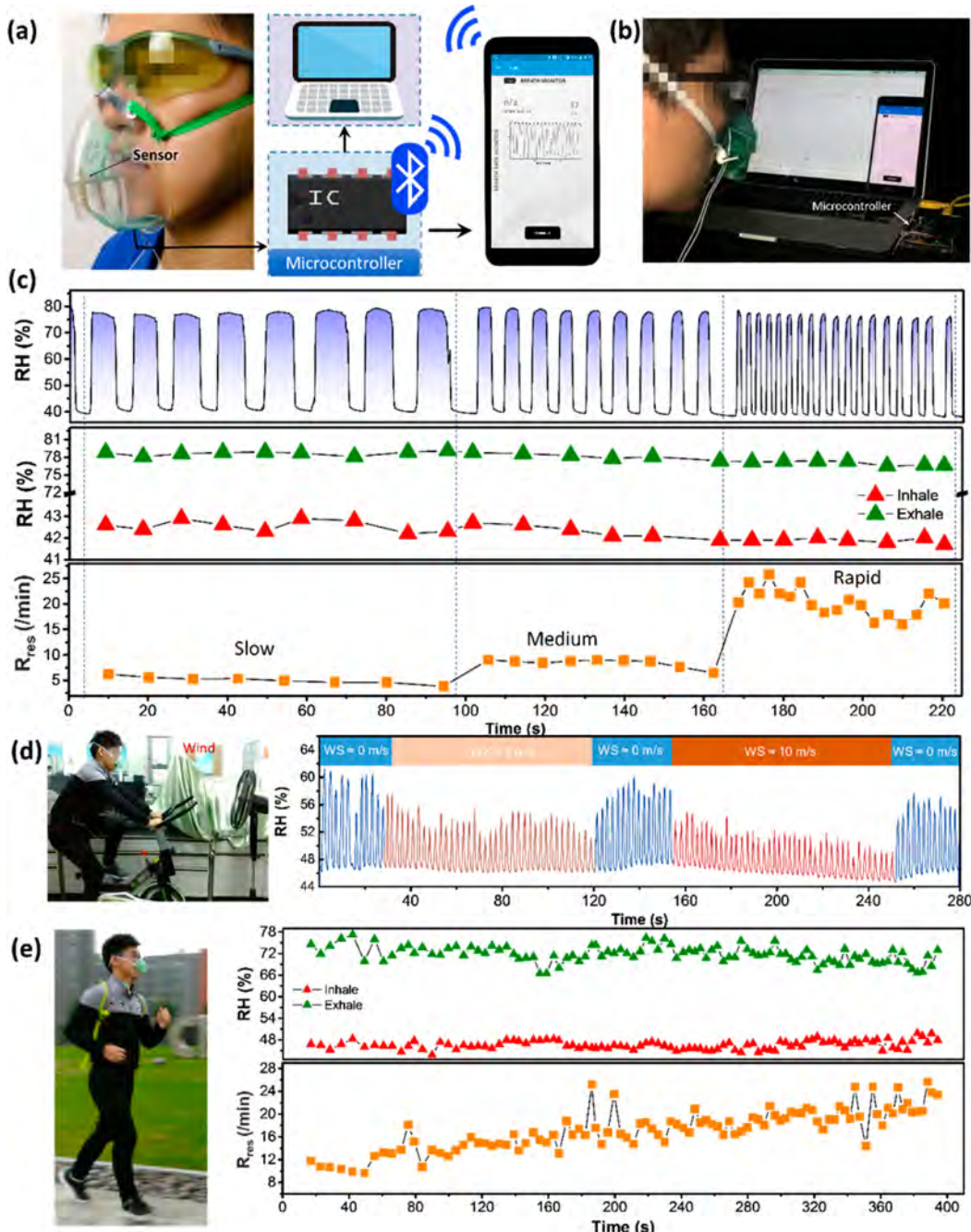


**Figure 5.** Humidity sensor application in human respiratory monitoring. (a) Image and schematic illustrations of the wearable human respiratory monitoring device system. (b) Photograph of the wearable device on a respiratory monitoring subject. (c) Raw respiratory signal recorded in 225 s with three different breathing states including slow, medium, and rapid and the obtained corresponding exhaled air RH value ( $RH_{Ex}$ ) and inhaled air RH value ( $RH_{Inh}$ ) and respiratory rate  $R_{res}$ . (d) Illustrations of the subject to test the effect of wind speed (WS) to breath signal. (e) Real-time respiratory monitoring results of a volunteer during an outdoor jogging exercise ( $\approx 3$  m/s).

performance of the device under wet ( $RH \approx 75\%$ ) and dry ( $RH \approx 35\%$ ) conditions (Figure S9). The raw signal respiratory curves are sharp and clear under both wet and dry conditions. Importantly, the sensing performance of our sensors is not affected when varying the distance between nose and the sensor (Figure S10). Therefore, we believe that the device can work well in most of our daily lives. Considering respiratory information is an important index to evaluate the training intensity and physiological condition of fitness enthusiasts and professional athletes in outdoor exercise, we further evaluate the effect of air flow to breath signal (Figure 5e). Although under

extreme conditions (wind speed  $\geq 10$  m/s) the fast air flow may mix with the exhaled air, which may further affect the exhaled air RH value, the breath signal is still sharp enough for the calculation of respiratory rate. The entire system can work well in most daily lives, thus delivering a practical wearable sensor technology that can be used for prolonged indoor and outdoor physical activities. As shown in Figure 5e, taking advantage of this high performance wireless respiratory monitoring device, we successfully monitored the respiratory signal of a volunteer during outdoor exercise in real time. We envision that the large cloud computing platform that could be collecting data through

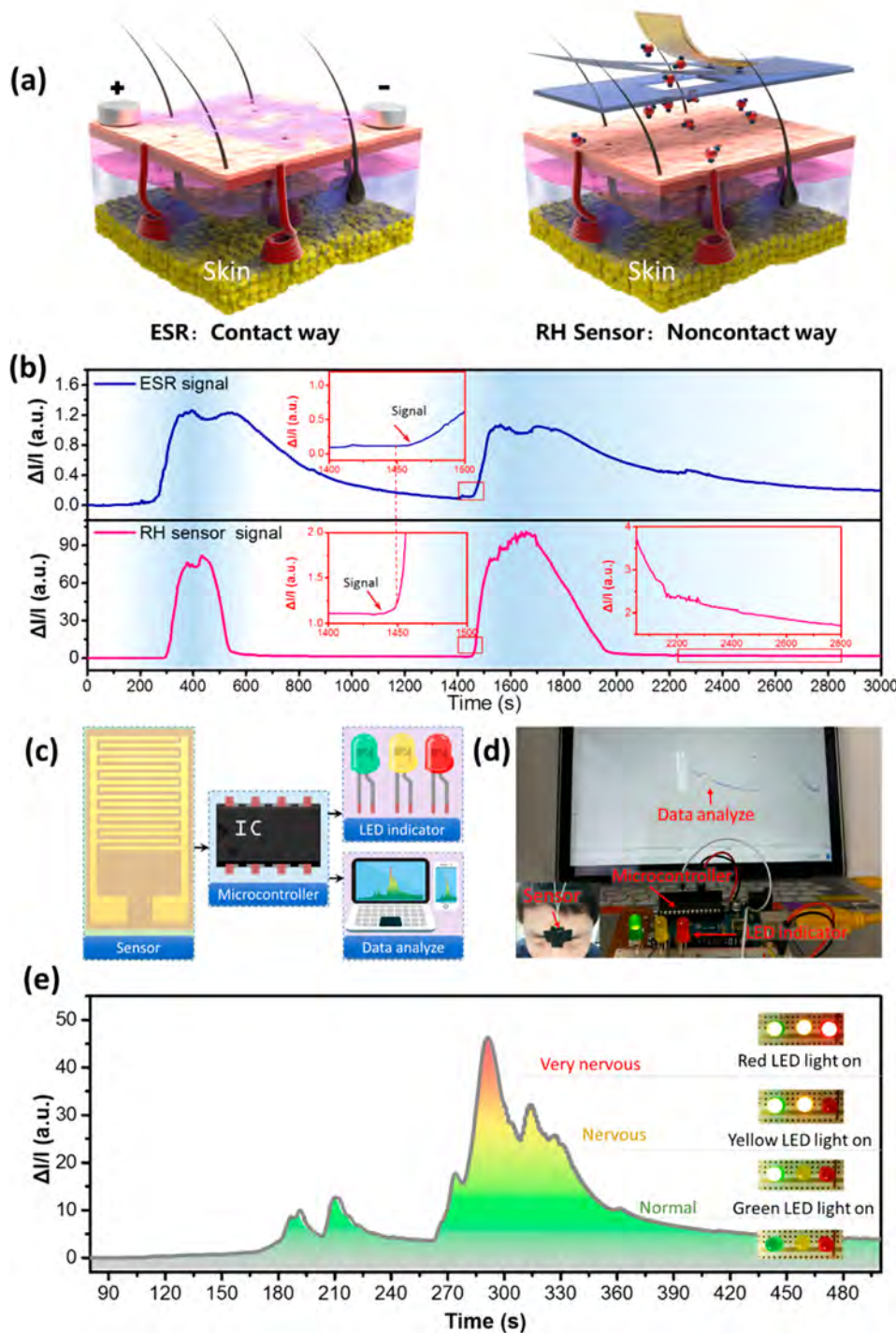


**Figure 6.** Real-time physiological and psychological monitoring: (a) proposed overview and system design of the wearable on-body real-time humidity analysis device. (b) Comparison of ESR signal and our RH sensor signal for skin activity monitoring during physical exercise of a volunteer. (c) Block diagram of the skin monitoring prototype (SMP) showing the RH signal transduction, microcontroller, LED indicator, and data analyzer (computer or mobile phone). (d) Photograph of the SMP system and its application for lie detection (e).

our device, along with voluntary community participation, would enable data-mining techniques with which to generate predictive algorithms for understanding the health status and clinical needs of individuals and society, which may provide valuable advice for our training and health improvement.

**Noncontact Human Skin Activity Real-Time Monitoring Device.** The human skin is the largest organ of the integumentary system. It not only plays an important immunity

role in protecting the body against pathogens and excessive water loss but also provides an opportunity for measuring human physiological and psychological parameters relevant to a wide range of conditions, diseases, health, and performance states in a continuous, real-time, and noninvasive manner.<sup>59</sup> For example, in early 1939,<sup>60</sup> Leonarde Keeler added galvanic skin response channel to his lie detector and patented it, because sweat gland activity is one of the most important physiological

parameters in the deception detecting process. Since then, Keeler's device was the first instrument purchased by the Federal Bureau of Investigation (FBI) and became the prototype for the modern polygraph.<sup>61</sup> Nowadays, numerous electrical skin resistance (ESR) devices have been created and widely used for the purpose of locating acupuncture points, diagnosis, treatment in the clinical practice, and monitoring the physiologic effect of physical activity.<sup>62</sup> To date, galvanic skin response is one of the few techniques used for skin activity monitoring. However, galvanic skin response is a very weak signal to detect, and worse the variable contact impedance between electrodes and tissue, the variation of pressure on electrodes, angle, or duration of the measurement can influence the results dramatically.<sup>63</sup> Thus, such approaches cannot support continuous, real-time measurements, therefore limiting their use to applications where stationary, infrequent tests are sufficient. As a result, further progress in this area will require new signal sources and hopefully allow for continuous and simultaneous sensing in noninvasive and noncontact ways.

Motivated by the ultrafast response and high sensitivity of the NPDA-RGO sensor, we fabricated an ultrahigh sensitive smart hand band to detect the subtle fluctuation of skin response through RH values on the skin surface (Figure S11). By fabricating sensors on a mechanically flexible polydimethylsiloxane (PDMS) substrate, a wearable and soft human skin RH real-time monitoring device was formed (Figure 6a). Compared to the ESR method for skin activity monitoring, our new device can detect weak signals with higher sensitivity in a noncontact way. As shown in Figure 6b, the RH sensor signal is nearly 100 times stronger than the ESR signal with little delay. Note that these signals were detected on the surface of wrist skin simultaneously during an elbow plank exercise. Taking advantage of our high performance device, it may provide new opportunities for accurate real-time skin activity monitoring during physical exercise in a noncontact way without considering the effect of contact impedance. The device was comfortably worn on various body parts, including wrists and forehead. Figure S12 shows a person wearing the smart device, packaged as a "smart wristband", allowing for real-time skin activity monitoring on the wrist simultaneously during mild exercise. During the exercise, the subtle change of human skin RH was recorded by external monitoring instruments and was found to increase with increasing time, as shown in Figure S13a. Interestingly, the skin RH increased very slowly and remained on a relatively low level during exercise (before 300 s). However, after the volunteer took a rest, the skin RH rose dramatically at about 400 s (probably because of muscle heat conductance to the skin surface, taking time for skin to respond) and then remained stable before it finally decreased gradually to its initial level. The human brain makes up 2% of a person's weight. Despite this, even at rest, the brain consumes 20–25% of the body's energy. The brain consumes energy at 10 times the rate of the rest of the body per gram of tissue, thus the brain is easily heated up and needs to be cooled down through skin by water evaporation.<sup>64</sup> This inspired us to develop a new noninvasive way to detect brain activity. By wearing the ultrahigh sensitive device on the forehead, packaged as a "smart head patch", we found that even the psychological activity can be monitored and studied simultaneously. The RH levels on the forehead during heavy brainwork followed similar trends to those obtained at wrist during physical exercise (Figure S13b). Interestingly, when an individual is in a relaxed state by listening to light music, the RH value on the forehead skin is not as stable as on the wrist. This is

probably because the brain is very active even in the absence of explicit input or output signals and consumes substantial energy and produces considerable heat even at rest.<sup>65</sup>

Furthermore, a lying person would sweat first on the forehead and then the dorsum of the hand, chest, and neck and least in the palm hand and finger of the skin than a truthful person.<sup>66,67</sup> Although the sweat signal forms on the forehead with least delay, most modern polygraphs detect galvanic skin response on the finger of the skin for its relatively stronger signal. Here, we designed a skin monitoring prototype (SMP) which can detect the weak and dynamical skin sweat gland activity on the forehead directly (Figure 6c and Figure 6d). Lying or psychological stress leads to excessive sweating on forehead skin immediately, and this subtle signal can be detected by the RH sensor and sent to the microcontroller and computer. As shown in Figure 6e, the tension level can be signified by different LED indicators, and the origin data was sent to a computer for further analysis (see Movie S3).

## ■ CONCLUSION

In conclusion, we have presented a GNCP nanofilm-based humidity sensor with high sensitivity, ultrafast response, and little hysteresis, which is quite suitable for continuous fast humidity fluctuation detection. The sensor design takes advantage of dynamic hydrogen bonds between PDA and water molecules, which results in a maximum resistance response of over 4 orders of magnitude toward moisture with an unprecedented response time (20 ms) and recover speed (17 ms) with little hysteresis. The fast response devices have been effectively employed for live monitoring of human speech and breath. The promising advantages of the sensing system then encouraged us to develop a new type of wearable health monitoring device, which can detect the subtlest change of RH on human skin and thus provide real-time physiological and psychological rich information on an individual in a noncontact way. Hence, this sensor delivers an opportunity for more accurate and more reliable ways for skin activity monitoring. In view of the facile preparation of the present humidity sensors and wearable health monitoring devices, we believe that this new concept of a bioinspired sensor based on weak hydrogen bond interactions may be applied in other molecular detection systems, which may be further generalized for the fabrication of wearable sensing systems for other important physiological parameters.

## ■ METHODS

**Reagents and Materials.** The giant GO nanosheets (10–30  $\mu\text{m}$ ) (Figure S1) were prepared by expansion, preoxidation, and oxidation according to our previously reported method.<sup>45</sup> Dopamine hydrochloride and Tris(hydroxymethyl)aminomethane were purchased from Sigma-Aldrich and used without further purification.

**Preparation of PDA-RGO.** 400 mL of homogeneous GO dispersion was mixed with 100 mL of Tris buffer solution ( $\text{pH} = 8.5$ ) with vigorous stirring for 2 h. Then, the dopamine hydrochloride was added slowly into the mixed solution in an ice bath with stirring for several minutes. After that, the reaction mixture was stirred at 40 °C for 24 h using the centrifugation washing method, and the PDA-RGO precipitate was repeatedly washed with deionized water for 6 d to remove free PDA particles and Tris for a clean PDA-RGO dispersion.

**Fabrication of GNCP Sensors.** An interdigitated Ni/Au interdigital electrode (IDE) was sputter-deposited on the PI substrate (Ni: 3  $\mu\text{m}$  thick; Au: 0.07  $\mu\text{m}$  thick). The IDE pattern on the PI substrate provided an outline dimension of 13 mm × 30 mm. Typical dimensions of the interdigitated electrodes were 150  $\mu\text{m}$  electrode

width, 150  $\mu\text{m}$  electrode separation, and 11 mm electrode length, and the number of electrodes was 42. (More details are available in Supporting Information Figure S2.) PDA-RGO aqueous solutions (0.01 g/L) were deposited onto the IDE coated PI substrate by drop casting. Drop casting was carried out using a micropipette (volume of deposited GO solution  $\sim$ 0.5 mL). After a slow drying process ( $\approx$ 12 h) in a closed vessel, the GNCP nanofilms are formed on substrate. The as-prepared sensor was connected to data acquisition and the computer to collect data. Thus, the sensing experimental setup was assembled successfully for further humidity testing experiments.

**Characterization.** Atomic force microscopy (AFM) images were taken by a multimode AFM (Being Nano-Instruments, Ltd.) operating in tapping mode using silicon cantilevers (spring constant: 0.15 N m $^{-1}$ , resonant frequency: 12 kHz for cantilever of contact mode, spring constant: 3–40 N m $^{-1}$ , resonant frequency: 75–300 kHz for cantilever of tapping mode). A Hitachi-S4800 field-emission scanning electron microscope (FE-SEM) was used to investigate the morphology of GO on silicon substrate. X-ray diffraction (XRD) patterns were collected on an AXS D8 Advance diffractometer with Cu K $\alpha$  radiation ( $\lambda = 1.5418 \text{ \AA}$ ). Fourier transform infrared spectroscopy (FTIR) was conducted through a Thermo Nicolet 6700 spectrometer in the 4000–400 cm $^{-1}$  frequency range, using thin film sample. The Raman scattering measurements were performed at room temperature on a Raman system (in Via-reflex, Renishaw) with confocal microscopy. The solid-state diode laser (532 nm) was used as an excitation source with a frequency range of 3200–1000 cm $^{-1}$ . The electrical impedance measurements were carried out using an electrochemical workstation CHI660E. Oscilloscope OWON HDS1021MN was used to measure the voltage drop across resistors. The temperature was measured using an IR camera JM500XC. The controlled humidity environments were achieved in a constant temperature ( $\sim$ 25 °C) and humidity room ( $\sim$ 50%). The environment temperature and humidity were monitored by using a hygrometer (TESTO 608-H2). The humidity environments were achieved using saturated aqueous solutions of pure N<sub>2</sub>, LiCl, CaCl<sub>2</sub>·6H<sub>2</sub>O, MgNO<sub>3</sub>, NaCl, and K<sub>2</sub>SO<sub>4</sub> in a closed glass vessel at an ambient temperature of  $\sim$ 25 °C, which yielded approximately 0%, 11%, 29%, 54%, 65%, 75%, and 97% relative humidity (RH), respectively. The flow rate for response speed test was about 400 sccm. The organic gas flows (ethanol, acetone, ethyl acetate, dimethyl sulfoxide, dichloromethane, hexane) were saturated vapor of each organic solvent at 20 °C. The Guilty Knowledge Test (GKT) and skin activity monitoring were operated in a constant temperature ( $\sim$ 20 °C) and humidity room ( $\sim$ 40%) for lie detection experiments according to the previously reported method.<sup>68</sup>

## ■ ASSOCIATED CONTENT

### Supporting Information

The Supporting Information is available free of charge on the ACS Publications website at DOI: [10.1021/acs.chemmater.8b01587](https://doi.org/10.1021/acs.chemmater.8b01587).

Detailed experimental procedures, characterization, and calculation: Figure S1, SEM image of the graphene oxide nanosheets; Figure S2, IDE pattern window on the PI substrate; Figure S3, AFM image of the layered structure GNCP film; Figure S4, Raman spectra of GNCP; Figure S5, XRD patterns of GNCP with different PDA weight ratios; Figure S6, long time stability of the GNCP sensor device; Table S1, high performance humidity sensors reported in the literature; theoretical study of the hydrogen bonds interaction between PDA and water molecules; Figure S7, PDA molecules “capture” water molecules through hydrogen bonds; Figure S8, processed respiratory RH curve signal with parameters marked for the respiratory data analysis; Figure S9, raw respiratory signal under dry atmosphere and wet atmosphere; Figure S10, raw respiratory signal tested by humidity sensor in different positions on the mask; Figure S11, sensor

response to RH on the surface of the skin; Figure S12, images and schematic illustrations the structure of the “smart wristband”; Figure S13, real-time physiological and psychological monitoring subject (PDF) Video 1, RH sensor response to speaking (AVI) Video 2, breath monitor (AVI) Video 3, lie detector (AVI)

## ■ AUTHOR INFORMATION

### Corresponding Authors

\*E-mail: [luwei@nimte.ac.cn](mailto:luwei@nimte.ac.cn) (W.L.).  
\*E-mail: [chys@nimte.ac.cn](mailto:chys@nimte.ac.cn) (Y.C.).  
\*E-mail: [tao.chen@nimte.ac.cn](mailto:tao.chen@nimte.ac.cn) (T.C.).

### ORCID

Wei Lu: [0000-0002-2803-9519](https://orcid.org/0000-0002-2803-9519)  
Patrick Théato: [0000-0002-4562-9254](https://orcid.org/0000-0002-4562-9254)  
Shiao-Wei Kuo: [0000-0002-4306-7171](https://orcid.org/0000-0002-4306-7171)  
Tao Chen: [0000-0001-9704-9545](https://orcid.org/0000-0001-9704-9545)

### Author Contributions

J.H., W.L., Y.S.C., and T.C. conceived and designed the experiments. J.H., J.W.S., and Y.L. performed the experiments. P.X. and J.W.S. contributed to materials. P.X., W.Q.W., P.T., and Y.S.C. contributed to characterization, analysis, and discussion. J.H., W.L., Y.S.C., P.T., S.W.K., and T.C. cowrote the paper.

### Notes

The authors declare no competing financial interest.

## ■ ACKNOWLEDGMENTS

This work was supported by the Natural Science Foundation of China (51573203, 51773214, 21404111, and 51503216), the Bureau of International Cooperation of Chinese Academy of Sciences (174433KYSB20170061), and Key Research Program of Frontier Science, Chinese Academy of Sciences (QYZDB-SSW-SLH036).

## ■ ABBREVIATIONS

PI, polyimide; PDA-RGO, poly(dopamine) modified reduced GO; GNCP, graphene nanochannels confined poly(dopamine); IDE, interdigital electrode; ESR, electrical skin resistance; PDMS, polydimethylsiloxane; SMP, skin monitoring prototype

## ■ REFERENCES

- (1) Gao, W.; Emaminejad, S.; Nyein, H. Y. Y.; Challa, S.; Chen, K.; Peck, A.; Fahad, H. M.; Ota, H.; Shiraki, H.; Kiriya, D.; Lien, D.-H.; Brooks, G. A.; Davis, R. W.; Javey, A. Fully Integrated Wearable Sensor Arrays for Multiplexed *In Situ* Perspiration Analysis. *Nature* **2016**, *529*, 509–514.
- (2) Takei, K. Nanowire Active-Matrix Circuitry for Low-Voltage Macroscale Artificial Skin. *Nat. Mater.* **2010**, *9*, 821–826.
- (3) Xu, S. Soft Microfluidic Assemblies of Sensors, Circuits, and Radios for The Skin. *Science* **2014**, *344*, 70–74.
- (4) Gong, S.; Schwalb, W.; Wang, Y.; Chen, Y.; Tang, Y.; Si, J.; Shirinzadeh, B.; Cheng, W. A Wearable and Highly Sensitive Pressure Sensor with Ultrathin Gold Nanowires. *Nat. Commun.* **2014**, *5*, 3132.
- (5) Wang, C. User-Interactive Electronic Skin for Instantaneous Pressure Visualization. *Nat. Mater.* **2013**, *12*, 899–904.
- (6) Rim, Y. S.; Bae, S.-H.; Chen, H.; De Marco, N.; Yang, Y. Recent Progress in Materials and Devices toward Printable and Flexible Sensors. *Adv. Mater.* **2016**, *28*, 4415–4440.
- (7) Choi, S.; Lee, H.; Ghaffari, R.; Hyeon, T.; Kim, D.-H. Recent Advances in Flexible and Stretchable Bio-Electronic Devices Integrated with Nanomaterials. *Adv. Mater.* **2016**, *28*, 4203–4218.

- (8) Liao, C.; Zhang, M.; Yao, M. Y.; Hua, T.; Li, L.; Yan, F. Flexible Organic Electronics in Biology: Materials and Devices. *Adv. Mater.* **2015**, *27*, 7493–7527.
- (9) Trung, T. Q.; Lee, N.-E. Flexible and Stretchable Physical Sensor Integrated Platforms for Wearable Human-Activity Monitoring and Personal Healthcare. *Adv. Mater.* **2016**, *28*, 4338–4372.
- (10) Sedó, J.; Saiz-Poseu, J.; Busqué, F.; Ruiz-Molina, D. Catechol-Based Biomimetic Functional Materials. *Adv. Mater.* **2013**, *25*, 653–701.
- (11) Hammock, M. L.; Chortos, A.; Tee, B. C. K.; Tok, J. B. H.; Bao, Z. 25th Anniversary Article: The Evolution of Electronic Skin (E-Skin): A Brief History, Design Considerations, and Recent Progress. *Adv. Mater.* **2013**, *25*, 5997–6038.
- (12) Perrier, E.; Vergne, S.; Klein, A.; Poupin, M.; Rondeau, P.; Le Bellego, L.; Armstrong, L. E.; Lang, F.; Stokey, J.; Tack, I. Hydration Biomarkers in Free-Living Adults with Different Levels of Habitual Fluid Consumption. *Br. J. Nutr.* **2013**, *109*, 1678–1687.
- (13) Minh, T. D. C.; Blake, D. R.; Galassetti, P. R. The Clinical Potential of Exhaled Breath Analysis for Diabetes Mellitus. *Diabetes Res. Clin. Pract.* **2012**, *97*, 195–205.
- (14) Smith, D.; Spanel, P. The Challenge of Breath Analysis for Clinical Diagnosis and Therapeutic Monitoring. *Analyst* **2007**, *132*, 390–396.
- (15) Wu, W.; Haick, H. Materials and Wearable Devices for Autonomous Monitoring of Physiological Markers. *Adv. Mater.* **2018**, *27*, 1705024.
- (16) Jin, H.; Abu-Raya, Y. S.; Haick, H. Advanced Materials for Health Monitoring with Skin-Based Wearable Devices. *Adv. Healthcare Mater.* **2017**, *6*, 1700024.
- (17) Mogera, U.; Sagade, A. A.; George, S. J.; Kulkarni, G. U. Ultrafast Response Humidity Sensor Using Supramolecular Nanofibre and Its Application in Monitoring Breath Humidity And Flow. *Sci. Rep.* **2015**, *4*, 4103.
- (18) Borini, S.; White, R.; Wei, D.; Astley, M.; Haque, S.; Spigone, E.; Harris, N.; Kivioja, J.; Ryhänen, T. Ultrafast Graphene Oxide Humidity Sensors. *ACS Nano* **2013**, *7*, 11166–11173.
- (19) Li, T.; Li, L.; Sun, H.; Xu, Y.; Wang, X.; Luo, H.; Liu, Z.; Zhang, T. Porous Ionic Membrane Based Flexible Humidity Sensor and its Multifunctional Applications. *Adv. Sci.* **2017**, *4*, 1600404.
- (20) Wang, Z.; Xiao, Y.; Cui, X.; Cheng, P.; Wang, B.; Gao, Y.; Li, X.; Yang, T.; Zhang, T.; Lu, G. Humidity-Sensing Properties of Urchinlike CuO Nanostructures Modified by Reduced Graphene Oxide. *ACS Appl. Mater. Interfaces* **2014**, *6*, 3888–3895.
- (21) Feng, J.; Peng, L.; Wu, C.; Sun, X.; Hu, S.; Lin, C.; Dai, J.; Yang, J.; Xie, Y. Giant Moisture Responsiveness of VS2 Ultrathin Nanosheets for Novel Touchless Positioning Interface. *Adv. Mater.* **2012**, *24*, 1969–1974.
- (22) Wang, X.; Xiong, Z.; Liu, Z.; Zhang, T. Exfoliation at the Liquid/Air Interface to Assemble Reduced Graphene Oxide Ultrathin Films for a Flexible Noncontact Sensing Device. *Adv. Mater.* **2015**, *27*, 1370–1375.
- (23) Hwang, S.-H.; Kang, D.; Ruoff, R. S.; Shin, H. S.; Park, Y.-B. Poly(vinyl alcohol) Reinforced and Toughened with Poly(dopamine)-Treated Graphene Oxide, and Its Use for Humidity Sensing. *ACS Nano* **2014**, *8*, 6739–6747.
- (24) Zhang, D.; Sun, Y. e.; Li, P.; Zhang, Y. Facile Fabrication of MoS<sub>2</sub>-Modified SnO<sub>2</sub> Hybrid Nanocomposite for Ultrasensitive Humidity Sensing. *ACS Appl. Mater. Interfaces* **2016**, *8*, 14142–14149.
- (25) Zhang, D.; Chang, H.; Li, P.; Liu, R.; Xue, Q. Fabrication and Characterization of an Ultrasensitive Humidity Sensor based on Metal Oxide/Graphene Hybrid Nanocomposite. *Sens. Actuators, B* **2016**, *225*, 233–240.
- (26) Zhang, D.; Tong, J.; Xia, B. Humidity-Sensing Properties of Chemically Reduced Graphene Oxide/Polymer Nanocomposite Film Sensor Based on Layer-By-Layer Nano Self-Assembly. *Sens. Actuators, B* **2014**, *197*, 66–72.
- (27) Zhang, D.; Tong, J.; Xia, B.; Xue, Q. Ultrahigh Performance Humidity Sensor Based on Layer-By-Layer Self-Assembly of Graphene Oxide/Polyelectrolyte Nanocomposite Film. *Sens. Actuators, B* **2014**, *203*, 263–270.
- (28) Lodish, H. *Molecular cell biology*; Macmillan: 2008; pp 29–47.
- (29) Jencks, W. P. *Binding Energy, Specificity, and Enzymic Catalysis: The Circe Effect*; Wiley Online Library: 1975; pp 219–410, DOI: 10.1002/9780470122884.ch4.
- (30) Kwon, O. S.; Song, H. S.; Park, S. J.; Lee, S. H.; An, J. H.; Park, J. W.; Yang, H.; Yoon, H.; Bae, J.; Park, T. H.; Jang, J. An Ultrasensitive, Selective, Multiplexed Superbioelectronic Nose That Mimics the Human Sense of Smell. *Nano Lett.* **2015**, *15*, 6559–6567.
- (31) Guo, L.; Yang, Z.; Dou, X. Artificial Olfactory System for Trace Identification of Explosive Vapors Realized by Optoelectronic Schottky Sensing. *Adv. Mater.* **2017**, *29*, 1604528.
- (32) Soler, M.; Newkome, G. R. Supramolecular Dendrimer Chemistry. In *Supramolecular Chemistry*; John Wiley & Sons, Ltd.: 2012; pp 29–47, DOI: 10.1002/9780470661345.smc138.
- (33) Lu, W.; Le, X.; Zhang, J.; Huang, Y.; Chen, T. Supramolecular Shape Memory Hydrogels: A New Bridge Between Stimuli-Responsive Polymers and Supramolecular Chemistry. *Chem. Soc. Rev.* **2017**, *46*, 1284–1294.
- (34) Zhang, X.; Wang, C. Supramolecular Amphiphiles. *Chem. Soc. Rev.* **2011**, *40*, 94–101.
- (35) Dang, V. Q.; Han, G.-S.; Trung, T. Q.; Duy, L. T.; Jin, Y.-U.; Hwang, B.-U.; Jung, H. S.; Lee, N.-E. Methylammonium Lead Iodide Perovskite-Graphene Hybrid Channels in Flexible Broadband Phototransistors. *Carbon* **2016**, *105*, 353–361.
- (36) Meng, H.; Xiao, P.; Gu, J.; Wen, X.; Xu, J.; Zhao, C.; Zhang, J.; Chen, T. Self-Healable Macro-/Microscopic Shape Memory Hydrogels Based on Supramolecular Interactions. *Chem. Commun.* **2014**, *50*, 12277–12280.
- (37) Novoselov, K. S.; Fal'ko, V. I.; Colombo, L.; Gellert, P. R.; Schwab, M. G.; Kim, K. A Roadmap for Graphene. *Nature* **2012**, *490*, 192–200.
- (38) Xiao, P.; Gu, J.; Chen, J.; Zhang, J.; Xing, R.; Han, Y.; Fu, J.; Wang, W.; Chen, T. Micro-Contact Printing of Graphene Oxide Nanosheets for Fabricating Patterned Polymer Brushes. *Chem. Commun.* **2014**, *50*, 7103–7106.
- (39) Allen, M. J.; Tung, V. C.; Kaner, R. B. Honeycomb Carbon: A Review of Graphene. *Chem. Rev.* **2010**, *110*, 132–145.
- (40) Geim, A. K. Graphene: Status and Prospects. *Science* **2009**, *324*, 1530–1534.
- (41) Chen, D.; Feng, H.; Li, J. Graphene Oxide: Preparation, Functionalization, and Electrochemical Applications. *Chem. Rev.* **2012**, *112*, 6027–6053.
- (42) Dong, L.; Yang, J.; Chhowalla, M.; Loh, K. P. Synthesis and reduction of large sized graphene oxide sheets. *Chem. Soc. Rev.* **2017**, *46*, 7306–7316.
- (43) Zhou, Y.; Bao, Q.; Tang, L. A. L.; Zhong, Y.; Loh, K. P. Hydrothermal Dehydration for the “Green” Reduction of Exfoliated Graphene Oxide to Graphene and Demonstration of Tunable Optical Limiting Properties. *Chem. Mater.* **2009**, *21*, 2950–2956.
- (44) Loh, K. P.; Bao, Q.; Ang, P. K.; Yang, J. The chemistry of graphene. *J. Mater. Chem.* **2010**, *20*, 2277–2289.
- (45) He, Y.; Wang, J.; Zhang, H.; Zhang, T.; Zhang, B.; Cao, S.; Liu, J. Polydopamine-modified graphene oxide nanocomposite membrane for proton exchange membrane fuel cell under anhydrous conditions. *J. Mater. Chem. A* **2014**, *2*, 9548–9558.
- (46) Liu, Y. L.; Ai, K. L.; Lu, L. H. Polydopamine and Its Derivative Materials: Synthesis and Promising Applications in Energy, Environmental, and Biomedical Fields. *Chem. Rev.* **2014**, *114*, 5057–5115.
- (47) Lee, H.; Dellatore, S. M.; Miller, W. M.; Messersmith, P. B. Mussel-Inspired Surface Chemistry for Multifunctional Coatings. *Science* **2007**, *318*, 426–430.
- (48) Li, Z.; Lu, W.; Ngai, T.; Le, X.; Zheng, J.; Zhao, N.; Huang, Y.; Wen, X.; Zhang, J.; Chen, T. Mussel-inspired multifunctional supramolecular hydrogels with self-healing, shape memory and adhesive properties. *Polym. Chem.* **2016**, *7*, 5343–5346.
- (49) He, J.; Xiao, P.; Zhang, J.; Liu, Z.; Wang, W.; Qu, L.; Ouyang, Q.; Wang, X.; Chen, Y.; Chen, T. Highly Efficient Actuator of Graphene/

- Polydopamine Uniform Composite Thin Film Driven by Moisture Gradients. *Adv. Mater. Interfaces* **2016**, *3*, 1600169.
- (50) Geissler, P. L.; Dellago, C.; Chandler, D.; Hutter, J.; Parrinello, M. Autoionization in Liquid Water. *Science* **2001**, *291*, 2121–2124.
- (51) Chen, Y.; Thorn, M.; Christensen, S.; Versek, C.; Poe, A.; Hayward, R. C.; Tuominen, M. T.; Thayumanavan, S. Enhancement of anhydrous proton transport by supramolecular nanochannels in comb polymers. *Nat. Chem.* **2010**, *2*, 503–508.
- (52) Nishihira, J.; Tachikawa, H. Theoretical Study on the Interaction Between Dopamine and its Receptor by ab initio Molecular Orbital Calculation. *J. Theor. Biol.* **1997**, *185*, 157–163.
- (53) Bayer, T.; Cunning, B. V.; Selyanchyn, R.; Nishihara, M.; Fujikawa, S.; Sasaki, K.; Lyth, S. M. High Temperature Proton Conduction in Nanocellulose Membranes: Paper Fuel Cells. *Chem. Mater.* **2016**, *28*, 4805–4814.
- (54) Ludueña, G. A.; Kühne, T. D.; Sebastiani, D. Mixed Grotthuss and Vehicle Transport Mechanism in Proton Conducting Polymers from Ab initio Molecular Dynamics Simulations. *Chem. Mater.* **2011**, *23*, 1424–1429.
- (55) Mäki-Ontto, R.; de Moel, K.; Polushkin, E.; Alberda van Ekenstein, G.; ten Brinke, G.; Ikkala, O. Tridirectional protonic conductivity in soft materials. *Adv. Mater.* **2002**, *14*, 357–361.
- (56) Bayer, T.; Bishop, S. R.; Perry, N. H.; Sasaki, K.; Lyth, S. M. Tunable Mixed Ionic/Electronic Conductivity and Permittivity of Graphene Oxide Paper for Electrochemical Energy Conversion. *ACS Appl. Mater. Interfaces* **2016**, *8*, 11466–11475.
- (57) Inoue, T.; Kamimae, J.-i.; Ueda, M.; Eguchi, K.; Arai, H. Ionic and Electronic Conductivities of La<sub>CoO<sub>3</sub></sub>- And LaMn<sub>3</sub>O<sub>6</sub>-Based Perovskite-Type Oxides Measured by the A.C. Impedance Method with Electron-Blocking Electrodes. *J. Mater. Chem.* **1993**, *3*, 751–754.
- (58) Shao, Y.; El-Kady, M. F.; Lin, C.-W.; Zhu, G.; Marsh, K. L.; Hwang, J. Y.; Zhang, Q.; Li, Y.; Wang, H.; Kaner, R. B. 3D Freeze-Casting of Cellular Graphene Films for Ultrahigh-Power-Density Supercapacitors. *Adv. Mater.* **2016**, *28*, 6719–6726.
- (59) Imani, S.; Bandodkar, A. J.; Mohan, A. M. V.; Kumar, R.; Yu, S.; Wang, J.; Mercier, P. P. A Wearable Chemical-Electrophysiological Hybrid Biosensing System for Real-Time Health and Fitness Monitoring. *Nat. Commun.* **2016**, *7*, 11650.
- (60) Trovillo, P. V. A History of Lie Detection. *Journal of criminal law and criminology (1931–1951)* **1939**, *29*, 848–881.
- (61) Grubin, D.; Madsen, L. Lie Detection and the Polygraph: A Historical Review. *J. Forensic Psychiatry & Psychology* **2005**, *16*, 357–369.
- (62) Kahneman, D.; Tursky, B.; Shapiro, D.; Crider, A. Pupillary, Heart Rate, and Skin Resistance Changes During a Mental Task. *J. Exp. Psychol.* **1969**, *79*, 164–167.
- (63) She, Y.-F.; Ma, L.-X.; Qi, C.-H.; Wang, Y.-X.; Tang, L.; Li, C.-H.; Yuan, H.-W.; Liu, Y.-Q.; Song, J.-S.; Zhu, J. Do Changes in Electrical Skin Resistance of Acupuncture Points Reflect Menstrual Pain? A Comparative Study in Healthy Volunteers and Primary Dysmenorrhea Patients. *Evid. Based Complement Altern. Med.* **2014**, *2014*, 836026.
- (64) Fox, M. D.; Raichle, M. E. Spontaneous Fluctuations in Brain Activity Observed with Functional Magnetic Resonance Imaging. *Nat. Rev. Neurosci.* **2007**, *8*, 700–711.
- (65) Lennie, P. The cost of cortical computation. *Curr. Biol.* **2003**, *13*, 493–497.
- (66) Chalmers, T. M.; Keele, C. A. The Nervous And Chemical Control of Sweating\*. *Br. J. Dermatol.* **1952**, *64*, 43–54.
- (67) Skolnick, J. H. Scientific theory and scientific evidence: An Analysis of Lie-Detection. *Yale Law J.* **1961**, *70*, 694–728.
- (68) Staunton, C.; Sean, H. An Investigation of the Guilty Knowledge Test Polygraph Examination. *J. Crim. Psych.* **2011**, *1*, 1–14.